CrossMark

Effects of Substitution of Fe by Mischmetal on Formation and Properties of Arc-Sprayed AlSi-Based Amorphous Coating

Qi Liu[1] · Jiangbo Cheng[1] · Baolei Wang[1] · Xiubing Liang[2]

Abstract The influence of a partial substitution of Fe with Mischmetal [$Ni_{60}RE_{40}$ (wt.%), RE: rare earth including Ce; La; Nd and Pr] on the glass formation ability (GFA), mechanical properties and electrochemical corrosion behavior of arc-sprayed AlSiFe-based amorphous coatings has been investigated. It is revealed that partial substitution of Fe by Mischmetal slightly debases the GFA and mechanical properties of the AlSiFe amorphous coating because of the selective oxidation of RE elements. With Mischmetal substitution, the amorphous fraction, onset crystallization temperature and microhardness of the coating decrease to 64.3%, 306 °C, and 338.7 Hv_{100}, respectively. Compared with a crystalline aluminum alloy and coating, the coating with Mischmetal substitution still has a prominent wear and corrosion resistance. The relative wear resistance of the coating with Mischmetal substitution is about 2.5 times than that of the 6061-Al alloy under the same dry sliding testing condition. In 0.6 M NaCl aqueous solution, the coating with Mischmetal substitution manifests a lower I_{corr}, higher E_{corr} and E_p values in polarization curves and bigger fitted R_{ct} value in EIS plots than does the as-sprayed crystalline Al coating.

✉ Jiangbo Cheng
chengjiangbo@hotmail.com

✉ Xiubing Liang
liangxb_d@163.com

1 College of Mechanics and Materials, Hohai University, Nanjing 211100, People's Republic of China

2 National Institute of Defense Technology Innovation, Academy of Military Sciences PLA China, Beijing 100010, People's Republic of China

Introduction

Al-based amorphous alloys, with their high strength-to-weight ratio, high elastic limit and excellent corrosion resistance (Ref 1-4), have been regarded as important structural and functional materials. As a result, there has been an unremitting interest of Al-based amorphous alloys ever since the discovery of Al-Si binary amorphous alloy in Ref 5. Unfortunately, although Al-based amorphous alloys have superior mechanical properties as compared to their conventional crystalline counterparts, material scientists and physicists still have faced the challenge to fabricate large size products due to their relatively low glass-forming ability (GFA) and very high cooling rates to avoid crystallization during solidification (Ref 6, 7). Up to day, the size limitation of Al-based amorphous alloys has obstructed their further potential applications as engineering materials (Ref 8, 9). To solve this thorny issue, it is highly desirable to further pursuit novel preparation processes for pushing engineering application of Al-based amorphous alloy.

Recently, thermal spraying techniques have furnished a flexible method for the synthesis of amorphous coatings because of their rapid cooling rate of $10^5 \sim$ K/s (Ref 10, 11). Numerous Al-TM (transition metal)-RE amorphous coatings have been prepared by spraying processes. Moreno et al. (Ref 12) investigated the corrosion resistance of Al-Co-Ce metallic glass coatings by pulsed thermal spray. The corrosion resistance of the Al-Co-Ce amorphous coating was improved by the release of ionic inhibitors to protect defects in the coating. Cold spraying process was

also reported as a suitable technique for large scale synthesis of $Al_{90.05}Y_{4.4}Ni_{4.3}Co_{0.9}Sc_{0.35}$ glassy coatings (Ref 13). The coating retained the glassy nature and exhibited excellent wear and corrosion resistance. Experiments by Henao et al. (Ref 14) showed that $Al_{88}Ni_6Y_{4.5}Co_1La_{0.5}$ metallic glass coatings with 81% of amorphous phase were fabricated by means of high pressure Cold Gas Spray technology. $Al_{86}Ni_6Y_{4.5}Co_2La_{1.5}$ amorphous metallic coating synthesized by high velocity air fuel spraying displayed 83.7% volume fraction of amorphous phase and low porosity of 0.12% (Ref 15). Among thermal spraying technologies, arc spraying is convenient, feasible and economical. It is extremely suitable for the fabrication of large area amorphous coatings because of rapid solidification rate and in most instances less expensive to operate than the other technologies (Ref 16, 17). In our previous research report, a novel Al-M (Metalloid)-TM (AlSiFe) metallic glass coating with the amorphous volume fraction of 74.9% was prepared by arc spraying process (Ref 18). It is well known that RE element in Al-based bulk metallic glass system is beneficial to improve its stability (Ref 19, 20). The GFAs of Al-based BMGs containing RE elements present a strong linear dependence on the size of the RE atom, i.e., larger RE atom facilitates glass formation. The atomic radii of Ce, La, Pr and Nd are 0.183, 0.188, 0.183 and 0.182 nm, respectively (Ref 1). Furthermore, the mixing enthalpies of Al-Ce, Al-La, Al-Pr, Al-Nd and Al-Ni are − 38, − 38, − 38, − 38 and − 22 kJ/mol, respectively, larger than that of Al-Fe (− 11 kJ/mol) (Ref 21). Considering that the larger atomic size difference and negative mixing enthalpy between the constituent elements are favorable for glass formation; thus, Mischmetal, namely Ni-based Mischmetal [$Ni_{60}RE_{40}$(wt.%)], may be a suitable substitution for Fe in the Al-Si-Fe alloys. However, it remains unclear how the GFA and mechanical properties will change when Fe is partially substituted by Mischmetal in an arc-sprayed Al-Si-Fe amorphous coating. So further research is needed on this topic.

Based on the above considerations, in this work, the effects of partially substituting Fe with Mischmetal on GFA as well as mechanical properties of arc-sprayed AlSiFe amorphous coatings were investigated. The microstructure and thermal stability of the coatings were characterized. Dry sliding wear behaviors and electrochemical properties of the coatings were also analyzed.

Experimental Procedures

A cored wire with 2 mm in diameter composed of pure aluminum strip outer skin wrapping alloy powders was employed as the precursor. Considering the electrical conductivity of the cored wire, Mischmetal ($Ni_{60}RE_{40}$: 60 wt.%
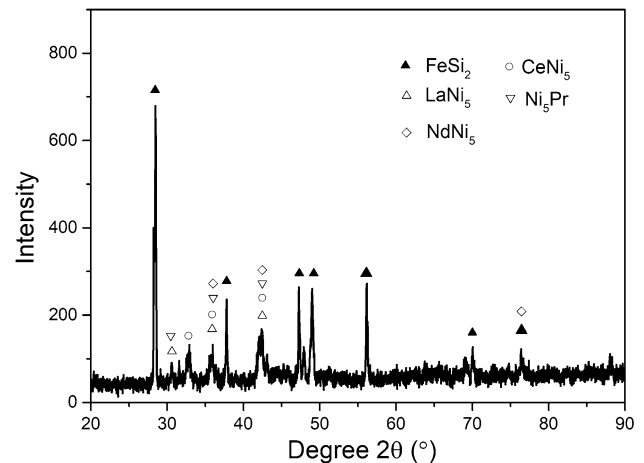

Fig. 1 XRD pattern of the powders

Ni; 20 wt.% Ce; 10 wt.% La; 8 wt.% Nd and 2 wt.% Pr) powders and ferro-silicon (75 wt.% Si and 25 wt.% Fe) powders were selected as filler alloy powders. Figure 1 shows the x-ray diffraction (XRD) pattern of the powders. Numerous sharp peaks appear in the XRD pattern of powders, indicating that the powders are crystalline in nature. The chemical composition of the cored wires is $(AlSi)_{90}$($Fe_{1−x}$ (Ni-RE)$_x$)$_{10}$ ($x = 0$, 0.7 at.%, nominal composition). The preparation process of the cored wires is the same as in Ref 18. Q235 steel (50 mm × 50 mm × 6 mm) was used as substrate. Before spraying, the substrates were degreased by acetone, dried in air and then grit-blasted. A high velocity arc spraying system was employed for coatings preparation (JZY-250, Beijing Jiazhiyuan Scientific & Trading Co., Ltd, China). To obtain high-quality coatings, the Laval nozzle was adopted to improve in-flight particles velocity. In order to evaluate the variation of the microstructure and properties with partial Mischmetal substitution, the arc-sprayed AlSiFe amorphous coating and pure Al coating were used as terms of comparison. The parameters for all coatings were as follows: spraying voltage 34 V, spraying current 150 A, compressed air pressure 0.7 MPa and the stand-off distance 200 mm.

The morphology of the coatings was examined by scanning electron microscopy (SEM, Carl Zeiss Microscopy GmbH, Germany) equipped with an energy dispersive x-ray analysis (EDXA, OXFORD instruments) apparatus. The microstructure was measured by transmission electron microscopy (TEM, Tecnai G2 F30 FEI Ltd., U.S.A.) and XRD. Differential scanning calorimetry (DSC) measurements of the coatings were carried out at a rate of 10 °C/min from 20 to 800 °C in N_2 atmosphere using a NETZSCH DSC 404 F3 differential scanning calorimeter instrument (NETZSCH Instruments Co., Ltd., Germany). Microhardness tests were conducted on the polished cross-sectional coatings and a bulk 6061-Al alloy with HVS-1000 Vickers hardness tester using a load of 100 g with 15 s loading time.

In order to obtain an average value, 15 indentations were randomly performed on the samples.

Dry sliding wear behaviors of the coatings and the bulk 6061-Al alloy were investigated by using a reciprocating ball-on-disk (Rtec, USA) tester at room temperature. A WC ball with a diameter of 12.7 mm was used as the sliding counterpart. Before wear testing, the surface of the tested samples was ground with mesh 4000 emery papers and then polished with W1.0 diamond paste until the roughness of the coatings; surface was lower than 1 μm. The normal load was set to be 15 N. The sliding velocity was 10 mm/s. The oscillating stroke was 2 mm, and the sliding testing time was 20 min. Before and after the sliding tests, all of the samples were cleaned in acetone solution. The worn surface was characterized using S3400 SEM, and wear volume loss of the samples was detected by a 3D non-contact surface mapping profiler (Olympus, LEXT OL 3000-IR).

The wear rates were calculated from the following equation (Ref 22):

$$W = \frac{V}{D \times L} \qquad \text{(Eq 1)}$$

where W is the wear rate in $mm^3/(N\,m)$, V is the wear loss volume in mm^3, D is the normal load in N, L is the sliding distance in m.

For electrochemical corrosion tests, all specimens were wet ground to P4000 finish, cleaned in acetone solution in an ultrasonic bath and dried with hot air. Electrochemical measurements were performed using an electrochemical cell, where an area of 1 cm^2 of the investigated samples was exposed to the naturally aerated 0.6 M NaCl solution open to air at 298 K after immersing the samples for 1 h. The tests were performed on a PARSTAT2273 electrochemical workstation (Princeton, USA) with a three electrode system. The system contains a saturated calomel reference electrode and a Pt counter electrode. Three types of electrochemical tests, namely open-circuit potential (OCP) test, potentiodynamic polarization test and electrochemical impendence spectroscopy test (EIS), were carried out to compare corrosion resistance of the AlSiFe coating, the AlSiFe coating with Mischmetal substitution and the crystalline pure Al coating. The immersion time of all OCP tests was set as 1800 s. The frequency range of EIS tests was from 10 kHz to 10 mHz, and the amplitude of sinusoidal potential signal was 5 mV with respect to the open-circuit potential. The EIS experimental data were fitted to appropriate equivalent circuits by ZSimpwin Commercial Software (USA) to get the significant R–C circuit parameters. Potentiodynamic polarization curves were examined in a potential range − 1.4 to 0.0 V with a potential sweep rate of 0.5 mV/s after immersing the samples for 1 h, when the open-circuit potential became steady. All tests were repeated at least thrice to ensure reproducibility.

Results and Discussion

Microstructure Characterization

The backscattered electron (BSE) images of the AlSiFe coating, the AlSiFe coating with Mischmetal substitution and the crystalline pure Al coating are shown in Fig. 2. From the overview image in Fig. 2(a), the as-sprayed AlSiFe coating with Mischmetal substitution exhibits lamellar structure because of the successive deposition of splats during arc spraying process. The steel substrate and the coating are adhering well, and there are no obvious microcracks in the bonding region. The thickness of the coating is about 560 μm. A magnified BSE micrograph of the AlSiFe coating with Mischmetal substitution is depicted in Fig. 2(b). The coating has a compact structure with well-flattened splats. Only a few microcracks exist in the coating, and partially round-like un-melted particles are present between the splats. The whole coating is divided into four color regions, namely white region, gray region, gray–black region and black region. The chemical compositions of these regions analyzed by EDXA are listed in Table 1. It is notable that the white regions are primarily RE-enriched oxide phases. These RE-enriched oxides distribute along the interfaces between flattened particles. The gray and gray–black regions are the coating alloy. It is worth noting that the contents of RE in the gray and gray–black regions are obviously lower than the designed value. The reason is that the flattened particles in the gray and gray–black regions are depleted in RE elements because of oxidation. In addition, some visible pores in the inter-splat areas appear as dark regions, see arrow in Fig. 2(a). The porosity of the coating is 2.3% by image analysis. The AlSiFe coating in Fig. 2(c) presents a denser structure with a porosity below 2%, i.e., lower than that of the AlSiFe coating with Mischmetal substitution. Figure 2(d) is the crystalline pure Al coating. Compared with the AlSiFe-based coating, the pure Al coating with many black big pores shows an incompact structure with a porosity of 2.7%. The chemical compositions of the whole AlSiFe coating (Fig. 2a) with Mischmetal substitution, the AlSiFe coating (Fig. 2c) and crystalline pure Al coating (Fig. 2d) measured by EDXA are $O_{9.25}Al_{66.54}Si_{13.3}Fe_{4.36}Ni_{4.49}Ce_{1.25}La_{0.64}Pr_{0.04}Nd_{0.13}$ (at.%), $Al_{76.01}Si_{13.51}Fe_{10.48}$ (at.%) and $O_{6.5}Al_{93.5}$ (at.%), respectively. It is noted that there is a higher oxygen content in the AlSiFe coating with Mischmetal substitution. This is mainly because the high velocity arc spraying is driven by compressed air. The in-flight particles are easily exposed to the air. It is inevitable that selective oxidation of the surface of droplets will appear during flight and deposition. The reaction enthalpies between O and the elements La, Ce, Pr and Nd
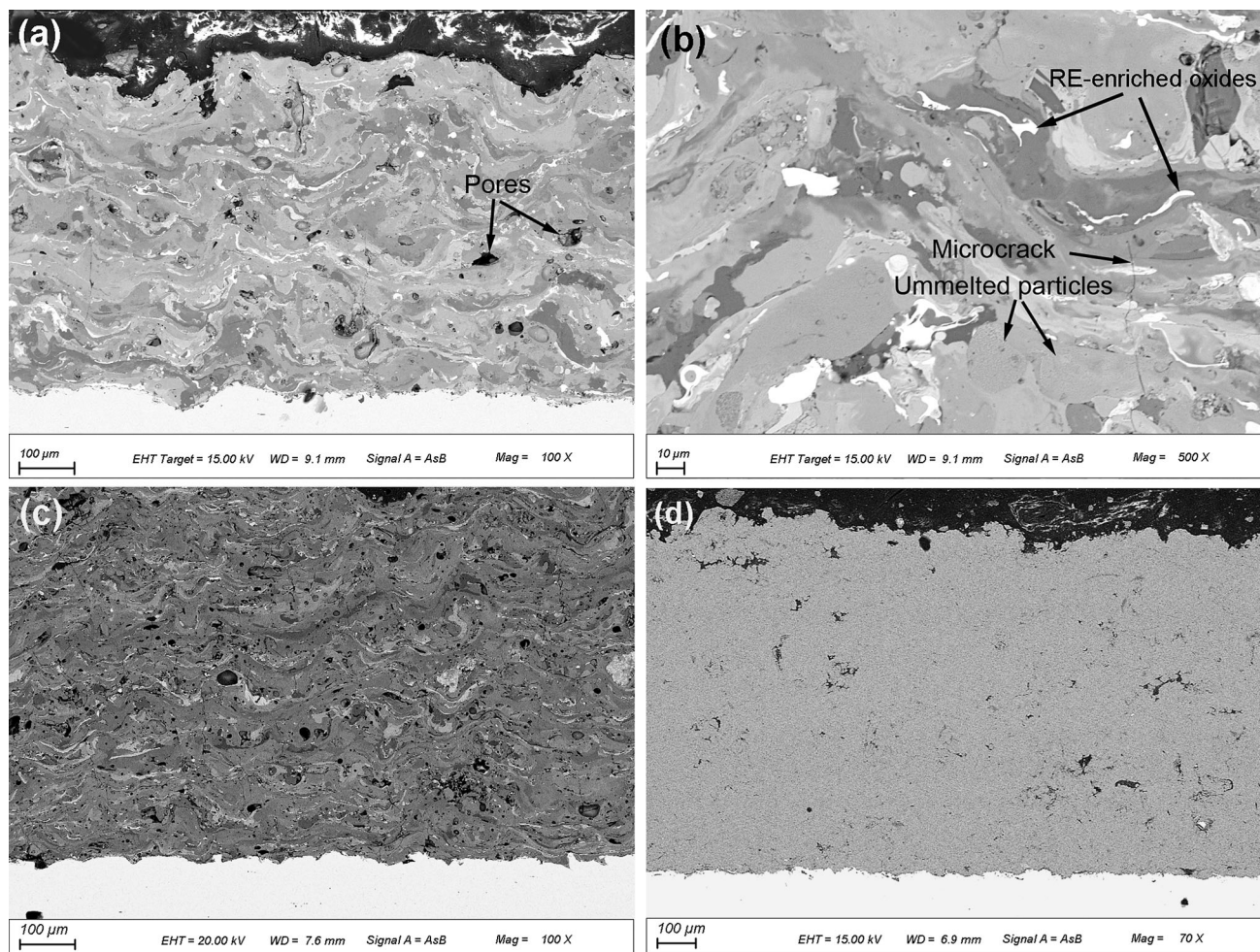
Fig. 2 BSE images of the coatings (a); (b) AlSiFe coating with Mischmetal substitution; (c) AlSiFe coating; and (d) Al coating

Table 1 The chemical compositions of the AlSiFe coating with Mischmetal substitution

Composition, at.%	O	Al	Si	Fe	Ni	Ce	Pr	Nd	La
White region	64.21	7.61	…	…	6	10.63	1.62	3.14	6.79
Gray region	…	71.7	18.44	4.81	4.38	0.32	…	0.35	…
Gray–black region	…	82.18	10.9	2.39	3.06	0.34	0.03	0.1	…

are − 1706, − 1729, − 1732 and − 1705 kJ/mol, respectively (Ref 23). The reaction enthalpies between O and the elements Al, Fe and Si are − 1597, − 725 and − 864 kJ/mol, respectively (Ref 23). These data show that the RE elements are the most reactive ones among the coating constituents. Therefore, preferred selective oxidation of RE elements occurs. However, those chemical compositions derived by EDXA have an indicative, semi-quantitative significance.

Figure 3 plots the XRD patterns of the AlSiFe coating and the AlSiFe coating with Mischmetal substitution. Both coatings show similar XRD patterns, indicating an amorphous hump at 30°-50° as well as some diffraction peaks of α-Al. It suggests that a small amount of nanometer-sized

Al crystals coexists in the amorphous matrix. But the width of the amorphous hump in the AlSiFe coating is greater than that of the AlSiFe coating with Mischmetal substitution. The volume fraction of the amorphous phase in the coating with Mischmetal substitution calculated by XRD method (Ref 24) is about 64.3%, which is lower than that of the AlSiFe coating, 74.9% (Ref 18). The corresponding DSC curves of the coatings and the cored wires are displayed in Fig. 4. There are no exothermic peaks for the DSC curves of both cored wires owing to the composition of crystalline alloy powders. The melting temperature (T_m) of the AlSiFe wire and Mischmetal-substituted AlSiFe wire is 643 and 647 °C, respectively. In the case of the coatings, there are some obvious exothermic crystallization
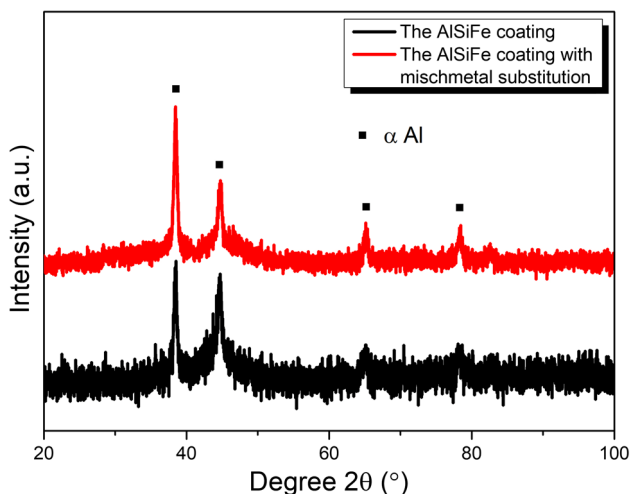
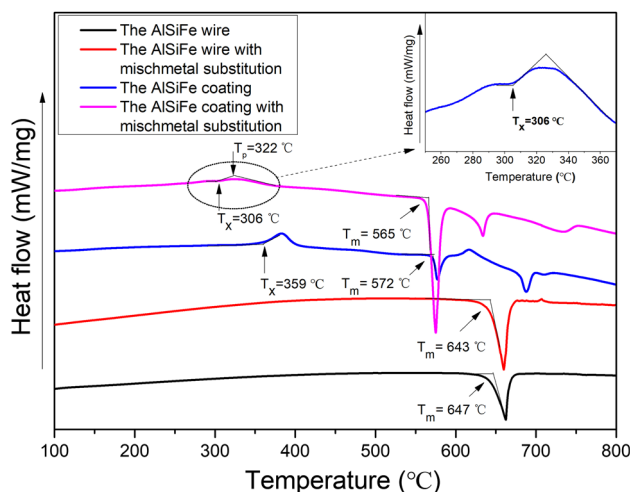Fig. 3 XRD patterns of the coatings

Fig. 4 DSC curves of the coatings and the cored wires

peaks in the curves, indicating the transitions from the amorphous phase to crystalline phases. No resolvable endothermic signals of both coatings associated with glass transition before crystallization are detected. The temperature for the onset of first crystallization (T_x) in the AlSiFe coating is 359 °C. However, with Fe partially substituted by Mischmetal, the exothermic peak weakens at the stage of crystallization. The values of T_x and peak temperature (T_p) of the AlSiFe coating with Mischmetal substitution are 306 and 322 °C, respectively, which are lower than those of the AlSiFe coating. The reason is that the preferred oxidation of RE elements on the surface of the in-flight droplets propelled by high pressure air during arc spraying triggers crystallization. In this case, the oxidation of metallic glass is an important problem for thermal processing because the oxidation would result in

heterogeneous nucleation sites and suppress the amorphous phase formation. Therefore, the prevention of oxide formation is entirely crucial to the synthesis of high amorphous fraction Al-based coating.

The TEM images and the selected area electron diffraction (SAED) patterns of the AlSiFe coating with Mischmetal substitution are shown in Fig. 5. The featureless contrast in the TEM image and the broad halo in the SAED pattern indicate a region with fully amorphous structure, as shown in Fig. 5(a). The chemical compositions of the "A" region marked in Fig. 5(a) are $Al_{84.11}Si_{6.49}Fe_{2.82}Ni_{4.91}La_{0.34}Pr_{0.26}Nd_{1.05}$ (at.%). Figure 5(b) is the nanoscale grains region of the coating. The diffraction spots validate the existence of crystals in the coating. It reveals mostly amorphous structure with a few nanocrystals ranging in size from 15 to 40 nm embedded in it. The nanoscale grains were identified as the α-Al phase from the polycrystalline SAED pattern shown in Fig. 5(b), and the chemical compositions of the nanoscale grain "B" region is $Al_{81.56}Si_{8.89}Fe_{2.91}Ni_{5.83}Ce_{0.26}Pr_{0.26}Nd_{0.26}$ (at.%). It is noted that the amorphous region contains larger rare metals amounts than the nanocrystalline region. Generally speaking, minor RE additions are left as the primary method to improve the GFA of the Al-based amorphous alloys owing to the large difference in atomic size and negative mixing enthalpy between the constituent elements (Ref 19, 20, 25). However, in comparison with previous findings on the AlSiFe metallic glass coating (Ref 18), it is concluded that the present AlSiFe coating with Fe partially substituted by Mischmetal has an extremely abnormal formation behavior of the glassy phase. The fact is that the GFA of arc-sprayed AlSiFe coating worsens with Mischmetal substitution. Although the explicit reason for such an abnormal behavior is unknown in the limited study, the following reasons may be considered. In arc spraying process, heating and melting occur when two electrically opposed charged metal wires are fed together in such a manner that a controlled arc occurs at the intersection. During dynamic and rapid metallurgical processes, heterogeneities in the chemical composition of molten droplets may depress the tendency to form glassy phase. In addition, arc spraying process utilizes high pressure air to propel the molten particles. The preferred selective oxidation of RE elements in the in-flight particles surface triggers crystallization. The RE-enriched oxides between splats confirm it, as seen in Fig. 2(b). Oxidation will deplete the content of RE in the present alloy (see the chemical composition of "B" region in Fig. 5b), which further worsens the GFA of the coating. Therefore, compared with the AlSiFe coating, the coating with Mischmetal substitution has a lower GFA.

Fig. 5 TEM images of the AlSiFe coating with Mischmetal substitution. (a) Amorphous region and (b) amorphous and nanocrystalline grains region. Inset SAED patterns are shown and exhibit diffuse rings (a), and spotty rings (b)
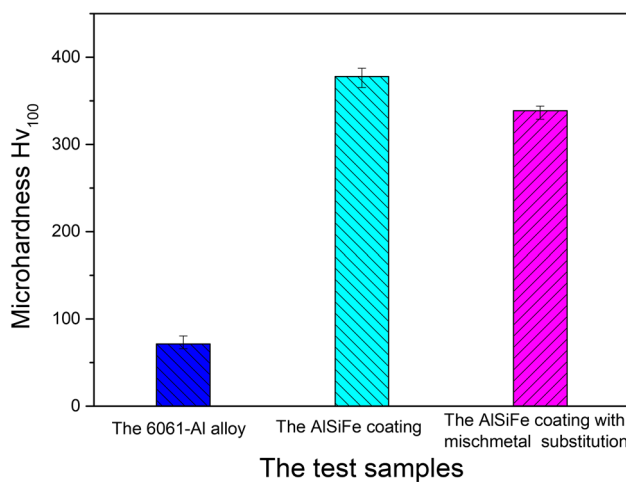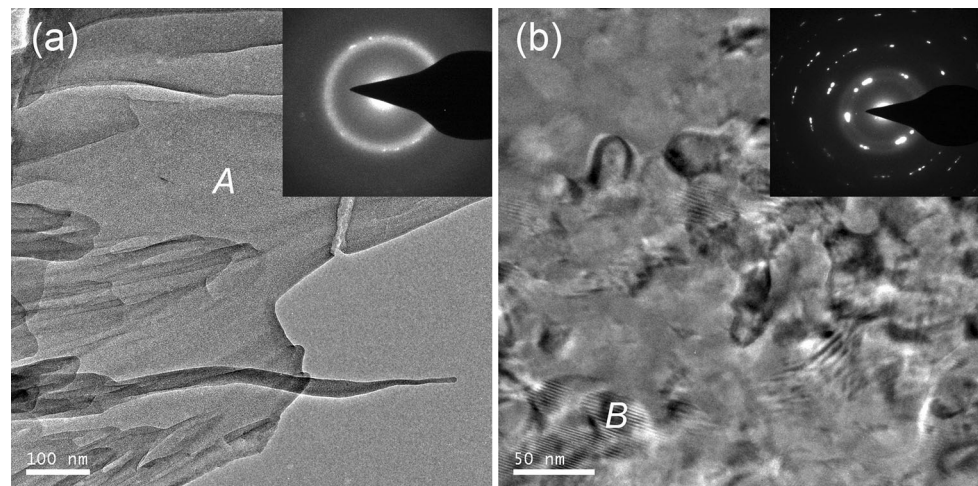

Fig. 6 Vickers hardness of the coatings and 6061-Al alloy

Fig. 7 Wear rates and coefficient friction of the coatings and 6061-Al alloy

Microhardness Evolution

Figure 6 illustrates the Vickers hardness of the coatings and 6061-Al alloy. Compared with the crystalline 6061-Al alloy, the amorphous coatings show higher hardness values. The hardness values of the AlSiFe coating and the AlSiFe coating with Mischmetal substitution are about 5.3 and 4.7 times that of the 6061-Al alloy, respectively. The high hardness of the AlSi-based amorphous coating is attributed to the results of the dense, randomly packed atomic structure of the glassy phase and strong bonding between the constituent elements. In addition, the hardness value of the AlSiFe coating decreases slightly with Mischmetal substitution. This is mainly ascribed to the decrease of the amorphous fraction and density of the coating with Mischmetal substitution.
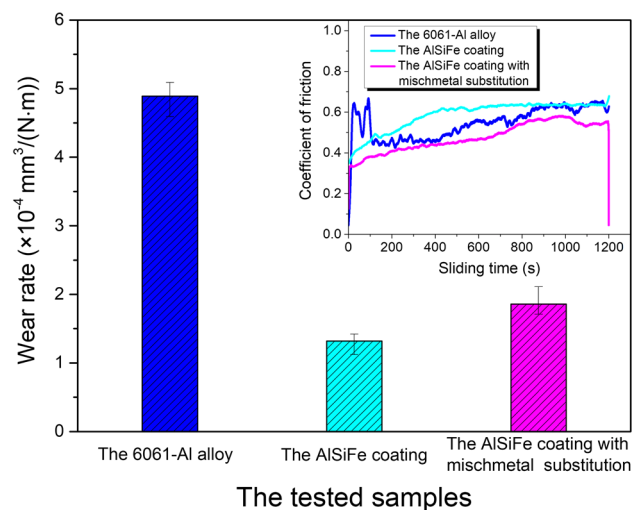
Tribological Behaviors of the Coatings

Figure 7 describes the wear rates of Al-based amorphous coatings and the 6061-Al alloy under normal load of 15 N, sliding speed of 10 mm/s and sliding time of 20 min. The average wear rate of the 6061-Al alloy is 4.89×10^{-4} mm^3 N^{-1} m^{-1}, while those of the AlSiFe coating and the AlSiFe coating with Mischmetal substitution are 1.32×10^{-4} and 1.95×10^{-4} mm^3 N^{-1} m^{-1}, respectively. The relative wear resistance of the AlSiFe coating and the AlSiFe coating with Mischmetal substitution is about 3.7 and 2.5 times that of the 6061-Al alloy, respectively. As Fe is replaced by Mischmetal, the wear rate of the coating shows a slight increase. The higher hardness

and amorphous fraction values provide the AlSiFe coating with higher resistance to plastic deformation, larger strain tolerance until final fracture and greater capability to absorb the applied deformation without exceeding the elastic limit or accommodate the deformation with less damage during the surface contact with the sliding WC ball, leading to the increase in wear resistance. The inset figure shows the coefficient of friction (COF) versus sliding time curves of the coatings and the 6061-Al alloy. The COF for the AlSiFe coating achieves a stable value of 0.65 after 400 s of sliding, whereas the coating with Mischmetal replacement produces a relatively lower COF value of 0.3-0.58. For the 6061-Al alloy, the COF value shows a large fluctuation in the range of 0.4-0.7. The large fluctuation of the friction coefficient is thought to be caused by the periodic localized fracture of the surface layer and accumulation or elimination of debris on the worn surface.

To explore the wear mechanism, the worn surface images of the samples after sliding testing are shown in Fig. 8. For the 6061-Al alloy, the worn surface is relatively rough and characterized by fragments delamination (Fig. 8a). Exfoliation of the surface material and numerous big craters are predominant on the surface of the 6061-Al alloy after dry sliding, indicating high material loss. The worn surface of the AlSiFe coating is smooth except for some small fragment delamination and bright compact tribological films (tribo-films). The chemical composition of these tribo-films marked as "A" region in Fig. 8(b) is $O_{62.86}Al_{24.18}Si_{6.98}Fe_{5.98}$ (at.%). In contrast, there are slacken tribo-flims with numerous cracks on the worn scar

of the AlSiFe coating with Mischmetal substitution, as shown in Fig. 8(c). The chemical composition of the "B" region marked in Fig. 8(c) is $O_{64.28}Al_{25.8}Si_{5.57}Fe_{1.36}$-$Ni_{2.58}Ce_{0.41}$ (at.%). It is demonstrated that the tribo-films consist of the oxides of the coatings and debris. By comparing Fig. 8(e) and (f), the 3D wear track profile of the AlSiFe coating with Mischmetal substitution is wider and deeper than that of the AlSiFe coating under the same sliding testing conditions. These further manifest the prominent wear resistance of the AlSiFe coating compared to the AlSiFe coating with Mischmetal substitution.

In order to investigate further the sliding wear behaviors of the tested samples, the cross section of the worn samples is presented. Figure 9(a) shows the subsurface of the 6061-Al alloy. The worn surface is covered with a layer, as shown by arrow in Fig. 9(a). The chemical composition of the "A" region in Fig. 9(a) is $Al_{58.33}O_{40.48}Mg_{1.18}$ (at.%). It is obvious that the layer consists of an oxidized tribo-film. Figure 9(b) is the cross-sectional morphology of the AlSiFe coating. There is a thin and continuous film on the worn surface. The chemical composition of the region marked "B" in Fig. 9(b) is $O_{28.71}Al_{53.5}Si_{11.75}Fe_{6.05}$ (at.%), which is consistent with that of the film of oxidized debris seen in Fig. 8(b). Simultaneously, the cross-sectional image of the AlSiFe coating seems smooth. No microcracks and serious plastic deformation appears on the subsurface. These phenomena confirm that the coating has excellent wear resistance. However, for the coating with Mischmetal substitution, a big spalling carter appears in the coating. Some longitudinal and traversal microcracks
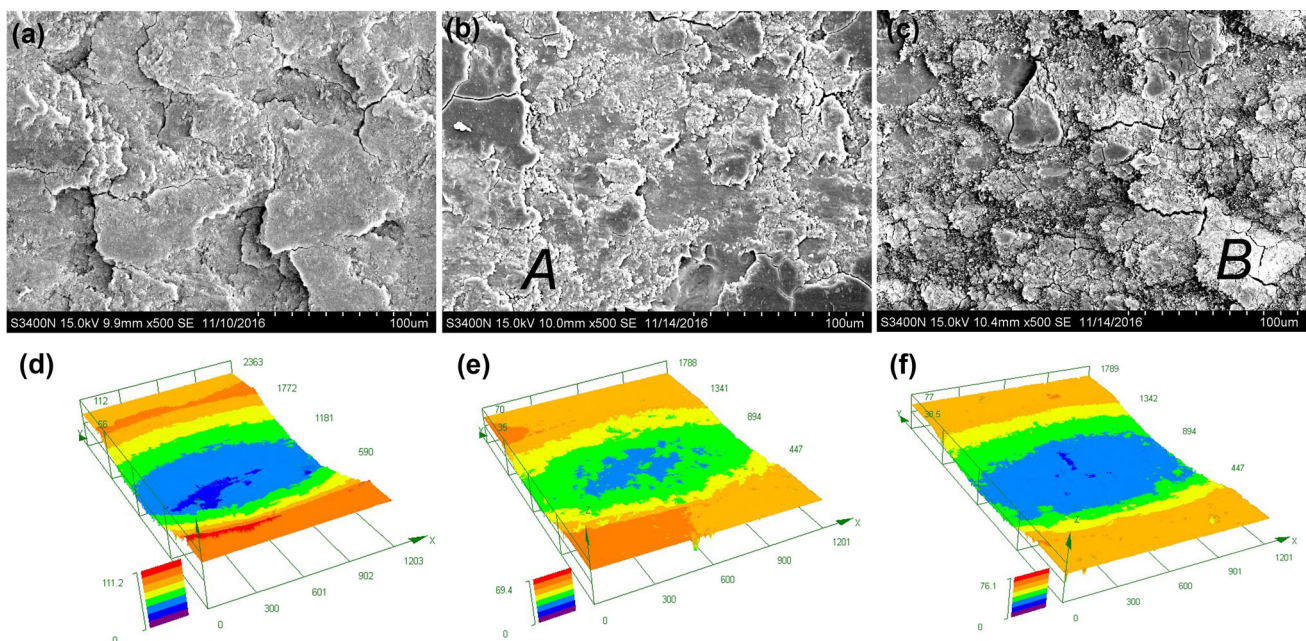

Fig. 8 SEM images and 3D profiles of the worn surface of the samples. (a), (d) for the 6061-Al alloy; (b), (e) for the AlSiFe coating; and (c), (f) for the AlSiFe coating with Mischmetal substitution
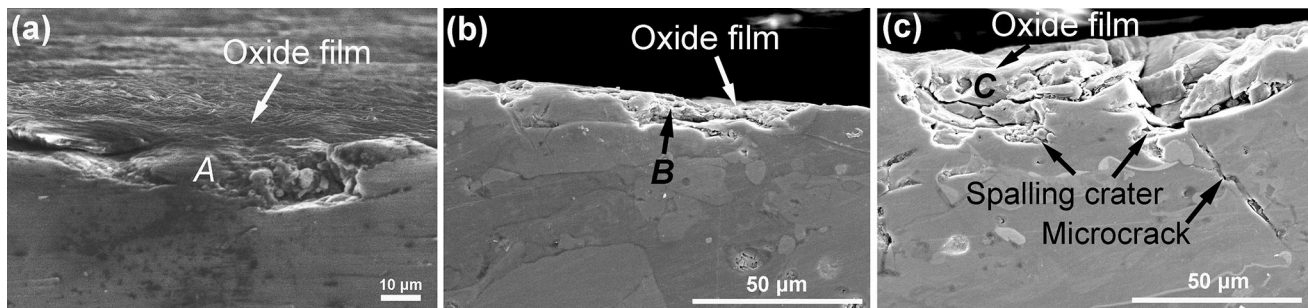
Fig. 9 SEM images of the cross section of the wear track on the samples. (a) 6061-Al alloy; (b) AlSiFe coating; and (c) AlSiFe coating with Mischmetal substitution
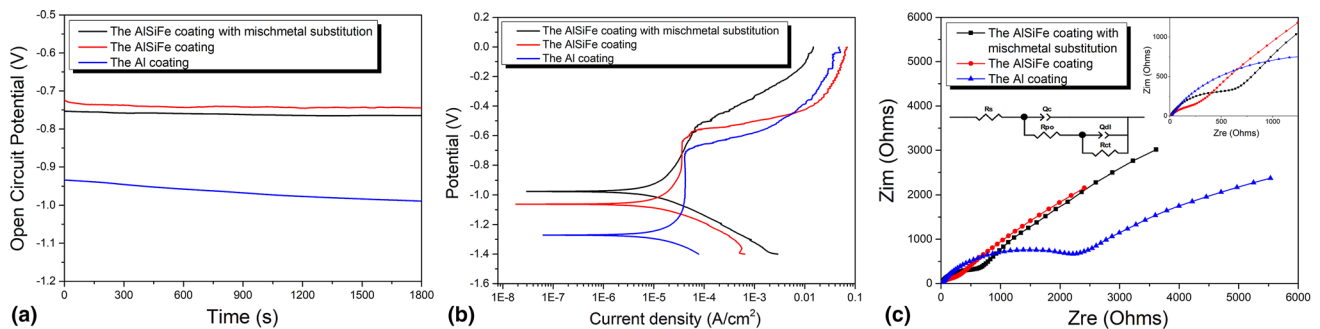

Fig. 10 OCP curves (a), potentiodynamic polarization curves (b), and Nyquist plots (c) of the coatings and the equivalent circuit model used to fit the EIS data depicted in (c)

propagate along the boundary between the flattened particles in the worn subsurface, as shown in Fig. 9(c). These features confirm that delamination is the dominant mechanism for the coating. Moreover, there is some dark layer covering the delamination crater, as shown by label "C" in Fig. 9(c). The chemical compositions of the "C" region are $O_{71.57}Al_{17.55}Si_{7.53}Fe_{2.59}Ni_{0.76}$ (at.%). It indicates that it is also the oxidative tribo-film. This evidence suggests that due to the dry sliding contact, wear particles are generated, they remain in the contact region being compacted and adhering to the surface of the counterpart and the coating, thus forming a chemically heterogeneous interfacial tribo-film. Under the effect of friction heat, tribochemical reactions occur during the formation of wear debris. With the repeated sliding action of WC ball, these oxidized debris experience compression and compaction leading to tribo-films.

Corrosion Behaviors of the Coatings

Figure 10(a) plots the OCP curves of the coatings immersed in 0.6 M NaCl solution for 1800s. For the arc-sprayed crystalline Al coating, the OCP curve slightly decreases from − 0.93 to − 0.99 V, while the OCP values of the AlSiFe amorphous coating and the AlSiFe

amorphous coating with Mischmetal substitution are around − 0.74 and − 0.76 V, respectively.

Figure 10(b) illustrates the potentiodynamic polarization curves of the coatings, while Table 2 summarizes relevant data. Both Al-based amorphous coatings show better overall general corrosion behaviors, with larger corrosion potential (E_{corr}), smaller corrosion current density (I_{corr}), higher pitting potential (E_p, the pitting potential is determined as the potential at which the slope of the I versus E curve changed suddenly at the end of the passive region, as shown in the polarization curves) and bigger polarization resistance (R_p) than that of the crystalline Al coating. With partial Fe replacement by Mischmetal, although E_{corr} and E_p are slightly improved, the higher critical passive current density (I_p) and I_{corr} values indicate that the passive film on the surface coating is less stable than that of the coating without Mischmetal substitution (Ref 26).

The Nyquist plots of the Al-based amorphous coatings and crystalline Al coating are depicted in Fig. 10(c) after 1 h of immersion in 0.6 M NaCl solution. It can be seen that all of the impedances have two depressed semicircles over the whole frequency range, and a considerable increase in the diameter of high-frequency capacitive arc is detected for the Al-based amorphous coating compared to

Table 2 The polarization diagram parameters of the coatings

The tested samples	E_{corr}, V	I_{corr}, μA/cm^2	E_p, V	I_p, μA/cm^2	R_p, Ω cm^2
The Al coating	− 1.272	14.58	− 1.231	13.888	4056.1
The AlSiFe coating	− 1.062	7.32	− 1.023	11.167	6097.5
The AlSiFe coating with Mischmetal substitution	− 0.976	9.82	− 0.909	12.643	5814.5

Table 3 The fitted results for EIS of the coatings

The samples	R_s, Ω cm^2	$Q_c - Yo$, F/cm^2	$Q_c - n$, F/cm^2	R_{po}, Ω cm^2	$Q_{dl} - Yo$, F/cm^2	$Q_{dl} - n$, F/cm^2	R_{ct}, Ω cm^2
The Al coating	11.41	3.75E−5	0.685	2446	9.61E−4	0.647	8373
The AlSiFe coating	5.36	2.19E−4	0.665	288.1	1.19E−3	0.561	2.04E−4
The AlSiFe coating with Mischmetal substitution	6.91	1.24E−4	0.778	739.8	1.19E−3	0.687	1.15E−4

the crystalline Al coating. Comparing the capacitive semi-arcs, the highest one is that of the AlSiFe amorphous coating followed by those of the AlSiFe coating with Mischmetal substitution and the crystalline Al coating. A bigger capacitive semi-arc is a signal of better corrosion resistance, which can also be acquainted with a higher charge transfer resistance and a lower I_{corr} and corresponds to a protective passive film formation on the coating sample (Ref 27). The equivalent electric circuit described in the inset of Fig. 10(c) is employed to model and fit the impedance parameters for all of the coatings. Considering the proposed equivalent circuit, the physical significance of the elements is that: R_s represents the solution resistance; R_{po} is the coating pore resistance; Q_c corresponds to the capacitance of the coating; R_{ct} and Q_{dl} are the interfacial charge transfer resistance and the double-layer capacitance, respectively. The fit values are listed in Table 3. Note that the R_{ct} value of the AlSiFe coating in 0.6 M NaCl solution is about 2.4 times and 1.8 times higher than that of the crystalline Al coating and the AlSiFe coating with Mischmetal substitution, respectively. It suggests that the AlSiFe coating has the best electrochemical behavior of all samples tested. Compared with the crystalline Al coating, the Al-based coatings with amorphous structure have prominent corrosion resistance because of the absence of crystalline defects such as grain boundaries, precipitates and segregation, which are favorable sites for corrosion, and the ability to form a perfect surface film (Ref 28, 29). However, the corrosion behavior of the Al-based amorphous coating primarily depends on the character of the structure. The AlSiFe coating has a denser structure, lower porosity and higher amorphous fraction than the AlSiFe coating with Mischmetal substitution, which is propitious

to the corrosion resistance. RE-enriched oxides, low amorphous fraction and incompact structure bear the responsibility of the relatively low corrosion resistance of the AlSiFe coating with Mischmetal substitution. To sum up, although the partial substitution of Fe by Mischmetal slightly decreases the GFA and mechanical properties of the coating, it still provides a potentially valuable guidance for expanding industrial applications.

Conclusion

1. The effect of partially substituting Fe by Mischmetal on the microstructure, GFA and mechanical properties of the AlSiFe coating was investigated in detail. Coatings were prepared by using arc spraying process.

2. The partial substitution of Fe by Mischmetal decreases the GFA and mechanical properties of the coating. With Mischmetal replacement, the amorphous fraction, onset crystallization temperature and microhardness of the coating decrease to 64.3%, 306 °C and 338.7 Hv100, respectively. The porosity of the AlSiFe coating with Mischmetal substitution increases to 2.3%. The wear and corrosion resistance of the coating also slightly decrease with Mischmetal replacement.

3. The AlSiFe coating with Mischmetal substitution still has a prominent wear and corrosion resistance comparison to the crystalline aluminum alloy and coating. The microhardness and relative wear resistance are about 4.7 and 2.5 times those of the 6061-Al alloy under the same testing conditions. In 0.6 M NaCl aqueous solution, the AlSiFe amorphous coating with Mischmetal substitution presents smaller I_{corr}, higher

E_p and R_{ct} values than the as-sprayed crystalline Al coating. The promising mechanical properties of the Al-based amorphous coating provide valuable guidance for expanding industrial applications.

References

1. A. Inoue, Amorphous, Nanoquasicrystalline and Nanocrystalline Alloys in Al-Based Systems, *Prog. Mater Sci.*, 1998, **43**, p 365-520

2. S.D. Zhang, Z.W. Liu, Z.M. Wang, and J.Q. Wang, In Situ EC-AFM Study of the Effect of Nanocrystals on the Passivation and Pit Initiation in an Al-Based Metallic Glass, *Corros. Sci.*, 2014, **83**, p 111-123

3. J. Yin, H. Cai, X. Cheng, and X. Zhang, Al-Based Bulk Metallic Glass with Large Plasticity and Ultrahigh Strength, *J. Alloys Compd.*, 2015, **648**, p 276-279

4. S. Kim, G. Lee, G. Park, H. Kim, A. Lee, S. Scudino, K.G. Prashanth, D. Kim, J. Eckert, and M. Lee, High Strength Nanostructured Al-Based Alloys Through Optimized Processing of Rapidly Quenched Amorphous Precursors, *Sci. Rep.*, 2018, **8**, p 1090. https://doi.org/10.1038/s41598-018-19337-7

5. P. Predecki, B.C. Giessen, and N.J. Grant, New Metastable Alloy Phases of Gold Silver and Aluminum, *Trans. Met. Soc. AIME*, 1965, **233**, p 1438-1439

6. Z.P. Chen, J.E. Gao, Y. Wu, H. Wang, X.J. Liu, and Z.P. Lu, Designing Novel Bulk Metallic Glass Composites with a High Aluminum Content, *Sci. Rep.*, 2013. https://doi.org/10.1038/srep03353

7. N.C. Wu, L. Zuo, J.Q. Wang, and E. Ma, Designing Aluminum-rich Bulk Metallic Glasses via Electronic-Structure-Guided Microalloying, *Acta Mater.*, 2016, **108**, p 143-151

8. Y. Shen and J.H. Perepezko, Al-Based Amorphous Alloys: Glass-Forming Ability, Crystallization Behavior and Effects of Minor Alloying Additions, *J. Alloys Compd.*, 2017, **707**, p 3-11

9. B.J. Yang, W.Y. Lu, J.L. Zhang, J.Q. Wang, and E. Ma, Melt Fluxing to Elevate the Forming Ability of Al-Based Bulk Metallic Glasses, *Sci. Rep.*, 2017, **7**, p 11053. https://doi.org/10.1038/s41598-017-11504-6

10. J.R. Davis, *Handbook of Thermal Spray Technology*, ASM International, Materials Park, OH, 2005

11. S.S. Joshi, S. Katakam, H.S. Arora, S. Mukherjee, and N.B. Dahotre, Amorphous Coatingsand Surfaces on Structural Materials, *Crit. Rev. Solid State Mater. Sci.*, 2015, **41**, p 1-46

12. F.P. Moreno, M.A. Jakab, N. Tailleart, M. Goldman, and J.R. Scully, Corrosion-Resistance Metallic Coatings, *Mater. Today*, 2008, **11**, p 14-23

13. D. Lahiri, P.K. Gill, S. Scudino, C. Zhang, V. Singh, J. Karthikeyan, N. Munroe, S. Seal, and A. Agarwal, Cold Sprayed Aluminum Based Glassy Coating: Synthesis, Wear and Corrosion Properties, *Surf. Coat. Technol.*, 2013, **232**, p 33-40

14. J. Henao, A. Concustell, I.G. Cano, S. Dosta, N. Cinca, J.M. Guilemany, and T. Suhonen, Novel Al-Based Metallic Glass Coatings by Cold Gas Spray, *Mater. Des.*, 2016, **94**, p 253-261

15. M. Gao, W. Lu, B. Yang, S. Zhang, and J. Wang, High Corrosion and Wear Resistance of Al-Based Amorphous Metallic Coating Synthesized by HVAF Spraying, *J. Alloys Compd.*, 2018, **735**, p 1363-1373

16. A.P. Newbery, P.S. Grant, and R.A. Neiser, The Velocity and Temperature of Steel Droplets During Electric Arc Spraying, *Surf. Coat. Technol.*, 2005, **195**, p 91-101

17. J. Cheng, S. Zhao, D. Liu, Y. Feng, and X. Liang, Microstructure and Fracture Toughness of the FePSiB-Based Amorphous/Nanocrystalline Coatings, *Mater. Sci. Eng. A*, 2017, **696**, p 341-347

18. J. Cheng, B. Wang, Q. Liu, and X. Liang, In-situ Synthesis of Novel Al-Fe-Si Metallic Glass Coating by Arc Spraying, *J. Alloys Compd.*, 2017, **716**, p 88-95

19. X.M. Shi, X.D. Wang, Q. Yu, Q.P. Cao, D.X. Zhang, T.D. Hu, L.H. Lai, H.L. Xie, T.Q. Xiao, and J.Z. Jiang, Structure Alterations in Al-Y-Based Metallic Glasses with La and Ni Addition, *J. Appl. Phys.*, 2016, **119**, p 1149041-1149049

20. W. Zhang, S.Q. Chen, Z.W. Zhu, H. Wang, Y.H. Li, H. Kato, and H.F. Zhang, Effect of Substituting Elements on Thermal Stability and Glass-Forming Ability of an Al-Based Al-Ni-Er Metallic Glass, *J. Alloys Compd.*, 2017, **707**, p 97-101

21. A. Takeuchi and A. Inoue, Classification of Bulk Metallic Glasses by Atomic Size Difference, Heat of Mixing and Period of Constituent Elements and Its Application to Characterization of the Main Alloying Element, *Mater. Trans.*, 2005, **46**, p 2817-2829

22. H. Kenneth and M. Allan, *Coatings Tribology: Properties, Mechanisms, Techniques and Applications in Surface Engineering*, 2nd ed., Elsevier Tribology Series, The Netherlands, 2009

23. D.L. Ye and J.H. Hu, *Practical Thermodynamics Data Handbook of Inorganic Substances*, Metallurgical Industry Press, Beijing, 2002

24. H.W. Yang, J. Wen, M.X. Quan, and J.Q. Wang, Evaluation of the Volume Fraction of Nanocrystals Devitrified in Al-Based Amorphous Alloys, *J. Non-Cryst. Solids*, 2009, **355**, p 235-238

25. Z. Zhang, X. Xiong, J. Yi, and J. Li, Effects of Substitution of La by Other Rare-Earth Elements on the Glass Forming Ability of $Al_{86}Ni_9La_5$ Alloy, *J. Non-Cryst. Solids*, 2013, **369**, p 1-4

26. A.M. Lucente and J.R. Scully, Pitting of Al-Based Amorphous-Nanocrystalline Alloys with Solute-Lean Nanocrystals, *Electrochem. Solid-State Lett.*, 2007, **10**, p C39-C43

27. S.S.A. Gillani and P. Häussler, Enhancement of Phase Stability by Manganese in $Al_{60-x}Mn_xCu_{40}$, *J. Non-Cryst. Solids*, 2018, **481**, p 361-367

28. W.R. Osório, D.J. Moutinho, L.C. Peixoto, I.L. Ferreira, and A. Garcia, Macrosegregation and Microstructure Dendritic array Affecting the Electrochemical Behaviour of Ternary Al-Cu-Si Alloys, *Electrochim. Acta*, 2011, **56**, p 8412-8421

29. J.B. Cheng, Z.H. Wang, and B.S. Xu, Wear and Corrosion Behaviors of FeCrBSiNbW Amorphous/Nanocrystalline Coating Prepared by Arc Spraying Process, *J. Therm. Spray Technol.*, 2012, **21**, p 1025-1031